Nanoscale

PAPER

View Article Online
View Journal | View Issue

Cite this: *Nanoscale*, 2022, **14**, 744

The synthesis and electrical transport properties of carbon/Cr_2GaC MAX phase composite microwires†

Jan P. Siebert,*[a] Debarati Hajra,*[b] Sefaattin Tongay [b] and Christina S. Birkel *[a,c]

Received 13th October 2021,
Accepted 13th December 2021

DOI: 10.1039/d1nr06780j

rsc.li/nanoscale

While MAX phases offer an exotic combination of ceramic and metallic properties, rendering them a unique class of materials, their applications remain virtually hypothetical. To overcome this shortcoming, a sol–gel based route is introduced that allows access to microwires in the range of tens of micrometers. Thorough structural characterization through XRD, SEM, EDS, and AFM demonstrates a successful synthesis of carbonaceous Cr_2GaC wires, and advanced low temperature electronic transport measurements revealed resistivity behavior dominated by amorphous carbon. The tunability of electronic behavior of the obtained microwires is shown by a halide post-synthesis treatment, allowing purposeful engineering of the microwires' electrical conductivity. Raman studies revealed the polyanionic nature of the intercalated halides and a slow decrease in halide concentration was concluded from time-dependent conductivity measurements. Based on these findings, the process is considered a viable candidate for fabricating chemiresistive halogen gas sensors.

Introduction

MAX phases are ternary transition metal-based carbides, nitrides and carbonitrides that crystallize in the hexagonal space group $P6_3mmc$ with the general chemical formula of $M_{n+1}AX_n$ (n = 1, 2, 3, 4).[1,2] M is an early transition metal, A mainly group 13 or 14 elements, and X is carbon and/or nitrogen. The M and X elements form octahedra (M_6X), that are intercalated with a single-atom layer of A. In so-called 211, 312 and 413 MAX phases, two, three and four layers of M alternate with one layer of the A element (indicated by n), respectively. Because of their unique crystalline structure and chemistry, MAX phases offer a combination of typical ceramic and metallic properties. Some examples for these are high thermal and electrical conductivity, chemical resistivity, oxidation resistance, damage tolerance, and fatigue resistance.[1] Recent studies have further predicted that these materials offer unique magnetic[3] and quantum properties such as ferromagnetic ordering.[4]

Despite their traditional and exotic properties, MAX phases are typically prepared by solid state reaction techniques which yield the target compounds in powder or pelletized form.[5–7] While these conventional methods are effective in producing MAX phases, they have their shortcomings especially for those compounds involving low melting point A atoms, such as Ga ($M_{n+1}GaX_n$). Achieving a homogenous or even decently mixed precursor mixture is shown to be a difficult task, for example for Ti_2GaC, Cr_2GaC, and Ti_4GaC_3.[8] Furthermore, these solid state techniques present great challenges in achieving more sophisticated and complex morphologies extending well beyond 0D nanoparticles or pelletized blocks. Hence, despite the tremendous progress in the micro and nanostructure based studies on other layered material systems,[9–11] low dimensional MAX phases still remain experimentally unexplored. Electronic and other properties of a material critically hinge on its dimension. Fascinating properties arising from the quantum confinement in 1D and 2D structures are routinely exploited in miniaturized new-generation devices.[12,13] Recently, 1D structures in the form of wires, rods and ribbons have shown a great promise to be used as advanced catalysts,[14] optical waveguides,[15,16] and sensors[17] due to their high aspect ratios. Enhanced surface area of 1D structures also adds another degree of freedom for tuning material properties by surface functionalization.[18] Therefore, to completely explore the MAX phases at low dimensions, there is a need to generate 1D ribbon or wire-like structures for added functionalities and easy integration into electronics, optics, energy conversion, and even quantum technology related fields.[19–21] Here, we report on the first demonstration of carbonaceous Cr_2GaC MAX phase microwires using sol–gel chemistry by both non-conventional microwave and conventional thermal heating

[a]*School of Molecular Sciences, Arizona State University Tempe, AZ-85287, USA. E-mail: christina.birkel@asu.edu*
[b]*Materials Science and Engineering, School for Engineering of Energy, Matter, and Transport, Tempe, AZ 85287, USA*
[c]*Department of Chemistry and Biochemistry, Technische Univesität Darmstadt, 64287 Darmstadt, Germany*

†Electronic supplementary information (ESI) available. See DOI: 10.1039/d1nr06780j

techniques. This approach introduces a scalable sol–gel chemistry route to produce 1D carbonaceous Cr_2GaC MAX wires, offering a viable and versatile alternative to conventional methods. Cryogenic electronic transport measurements performed on these wires show that these microwires exhibit classical metallic, insulating-like, as well as a unique non-monotonic temperature dependence. Subsequent bromine and iodine halide treatment on these wires enables us to further reduce the electrical resistivity and time-resolved conductivity measurements offer fundamental insights into the halide treatment process.

Results and discussion

A typical synthesis was based on 2.5 g of dextran (average molecular weight: 75k M, Alfa Aesar) dissolved in 2.5 mL deionized water containing the metal precursors. The metal precursors were $Cr(NO_3)_3{\cdot}9H_2O$ (Honeywell, 98%) and $Ga(NO_3)_3{\cdot}2H_2O$ (Alfa Aesar, 99.9%) and were weighed in air. The optimal concentration of the metal ion precursor solution was found to be 1.7 mmol mL^{-1}. This translates, for a 2.5 g dextran synthesis, into 1.1337 g of chromium nitrate and 0.4181 g of gallium nitrate, giving a Cr : Ga ration of 2 : 1. The precursors were dissolved in 2.5 mL DI water prior to adding 2.5 g of dextran, which was stirred in once the metal precursors were entirely dissolved. Upon complete incorporation of dextran, the as-obtained, viscous, deep-violet solution was rested overnight at room temperature. This process resulted in a slightly hardened and sticky gel, which subsequently was used to spin wires, using two glass microscopy slides. A small amount of gel was applied to a slide and spread out using the second slide by applying firm pressure. Pulling the slides apart quickly resulted in spontaneous formation of multiple wires, which, depending on the amount used, could be easily pulled into lengths greater than one meter. The wires were stretched over a Petri dish and dried overnight at 100 °C. After drying, the wires changed color from a violet hue to a brownish yellow. Using an alumina crucible, the wires were heated under flowing argon with a heating rate of 2 °C min^{-1} to 1050 °C, and held at that temperature for 2 hours before cooling to room temperature (tube furnace EST, Carbolite).

In case of microwave assisted synthesis, a setup similar to previously reported works has been used,[22,23] with a modification allowing to run Ar into the reaction chamber during the heating process. A quartz tube was used to guide argon into the reaction through an opening in the top of the microwave housing. Wires combusted in the setup were placed in an alumina tube, which was evacuated and flushed with Ar three times, embedded in 7 g of graphite granules (activated charcoal, DARCO, 12-20 mesh, Honeywell) in the insulation housing (alumina fiber boards, Skyline Components LLC), and flushed for 15 minutes prior to heating it under flowing Ar (0.25 LPM). The microwave (Mars 6, CEM Corporation) was set to 700 W and was run for 20 minutes. A sample preparation scheme is illustrated in Fig. 1.

Structural understanding of 1D MAX wires

The process, outlined above, produced Cr_2GaC MAX phase wires with well-rounded curvatures and diameters ranging from a few to tens of micrometers as shown in the SEM images in Fig. 2a and 3a. As-synthesized wires were structurally characterized using laboratory-scale X-ray powder diffraction (D2 Phaser 2nd Generation, Bruker), and to minimize anisotropic effects as much as possible, the samples were ground into a powder using an agate mortar. All data were refined using the Rietveld method and Topas.[24] Both synthesis strategies resulted in mainly Cr_2GaC wires, with Cr_3C_2 as the dominant side phase (6–14 wt%). Interestingly, furnace wire samples exhibit a more amorphous character compared to microwave wires, clearly visible in the higher noise level in Fig. 2c compared to Fig. 3c. Starting with furnace-derived

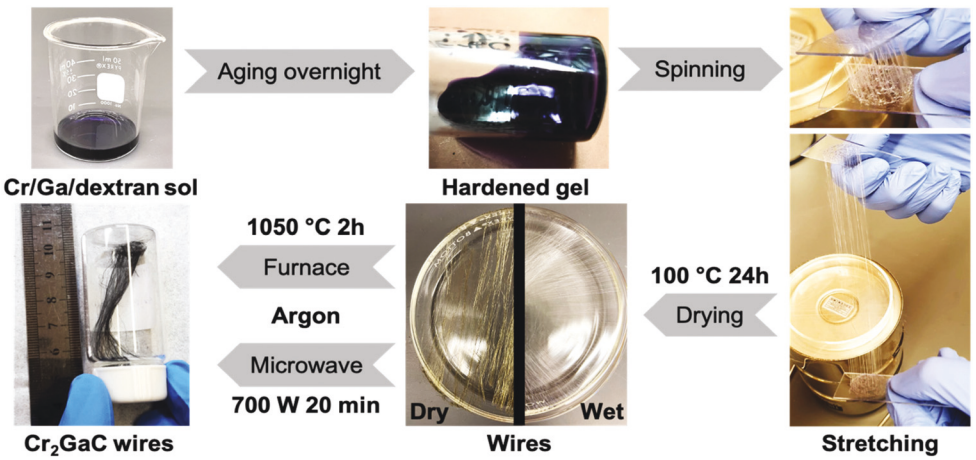

Fig. 1 Schematic illustrating the process of preparing Cr_2GaC microwires from gel precursor (top left) to spun wires (right) by means of photographs. The bottom center shows the wires pre- and post-drying, and the bottom left shows the final product after annealing in Ar, either *via* conventional heating or microwave heating.

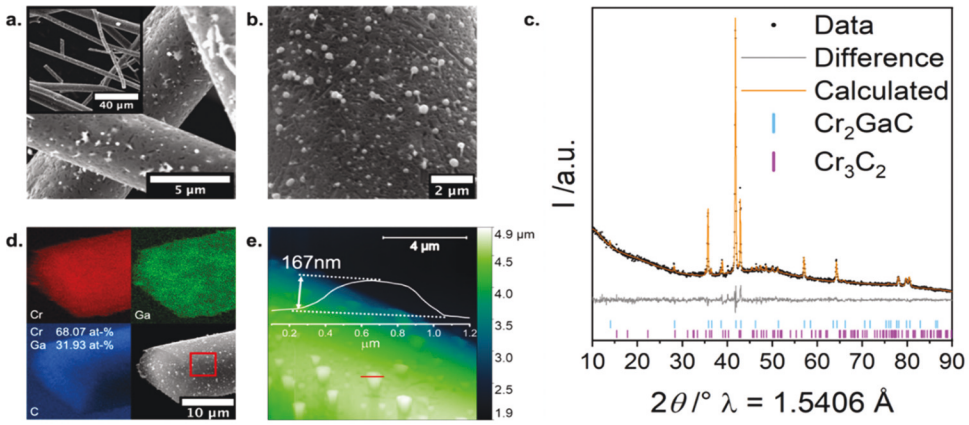

Fig. 2 a. SEM micrograph showing multiple wires. Inset showing an overview micrograph demonstrating the variance in diameter. b. SEM micrograph showing the surface morphology of the furnace-derived microwires; c. Rietveld refinement of furnace-derived Cr_2GaC XRD data, fitted with structural models of Cr_2GaC and Cr_3C_2; d. SEM EDS elemental analysis showing the uniform distribution of Cr, Ga, and C, as well as the expected 2 : 1 ratio of Cr : Ga; e. AFM data (10 × 10 µm) showing the surface depositions as well as an extracted profile (red line, profile overlaid in white), with the determined height of 167 nm.

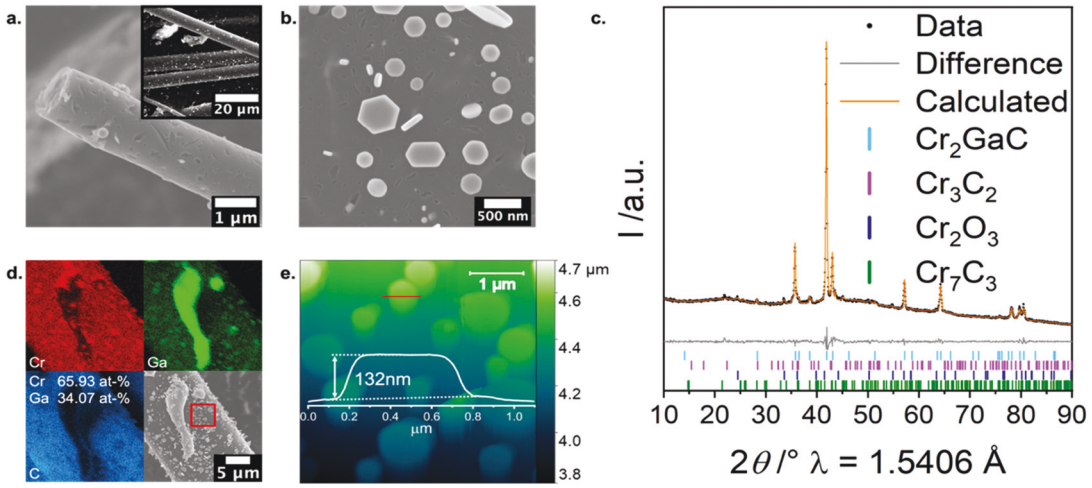

Fig. 3 a. SEM micrograph showing a microwave-derived wire. Inset showing multiple micrographs at lower magnification; b. SEM micrograph showing the surface morphology of the microwave-derived microwires, including hexagonally shaped particles; c. Rietveld refinement of microwave-derived Cr_2GaC XRD data, fitted with structural models of Cr_2GaC, Cr_7C_3, Cr_2O_3, and Cr_3C_2; d. SEM EDS elemental analysis showing the uniform distribution of Cr, Ga, and C around the Ga-segregations sitting on top of the wire surface, as well as the expected 2 : 1 ratio of Cr : Ga based on the indicated area (red square); e. AFM data (4 × 4 µm) showing the surface depositions as well as an extracted profile (red line, profile overlaid in white), with the shape of the deposition being more rectangular than in Fig. 2e.

wires (FW), the phase analysis revealed 86.2 wt% Cr_2GaC and consequently 13.8 wt% Cr_3C_2, confirming the successful synthesis suggested by the XRD pattern. Microwave-derived wires (MW) exhibit a similar yield for the MAX phase (82.1 wt%), however, two more side phases aside from Cr_3C_2 (6 wt%) are found: Cr_7C_3 (5.8 wt%) and Cr_2O_3 (5.5 wt%), as presented in Fig. 3a. For full details and results of the refinement, see ESI (Tables S1–S6†). SEM and EDS studies were carried out to shed light on size, length, and morphology of the obtained wires.

As shown in Fig. 2a, the diameter of furnace-derived wires ranges from sub-microns up to about 60 µm, which is the same for microwave-derived wires (see Fig. 3a). Hence the method of combustion has no effect on the average diameter, it is fully determined by the spun, pre-combustion wire diameter. The spinning process also results in fused wires of random diameters (see Fig. S3†). In the following, we will present the differences between MW and FW in terms of their chemical distribution/microstructure in detail in order to then provide a full discussion on their properties.

The surface morphology of the differently annealed wires differs quite significantly. While FW show a very cratered/scarred outer layer, MW exhibit a smoother, less disrupted, partly even closed surface. This is a counterintuitive observation since the significantly faster reaction times and faster emission of gaseous byproducts during the microwave treatment should lead to a more porous wire surface. In both cases,

the surface of the wires is decorated with smaller MAX phase particles in the nm – range (as confirmed by EDS analyses, Fig. 2d and 3d), which makes sense based on the sol–gel based synthesis that involves many small nuclei. Based on EDS quantification, and in contrast to the XRD results, the wires contain a significant amount of carbon (about 96 and 92 at% for FW and MW, respectively). As this carbon is not visible in XRD, it presents amorphous graphite.

Using AFM, these surface deposited particles were investigated in greater detail. Based on the data shown in Fig. 2e, FW depositions have an average height of 131.2 (±41.8) nm, which is very similar to the average height of MW particles (137.5 ± 46.5 nm, Fig. 3e).

For the MW, the surface particles are less droplet-like, and in significant numbers, even hexagonally shaped (see Fig. 3b, AFM profile Fig. 3e) particles. Based on the SEM investigation of the wires, the known side phase Cr_3C_2 must be perfectly mixed into the wire surface, on a very small scale, as high spatial resolution EDS could not identify single Cr_3C_2 particles. However, the MW exhibit a few randomly distributed Ga segregations on the wire surface (see Fig. 3d), confirmed by line scans performed across those segregations (Fig. S3†). The presence of elemental Ga could have two possible explanations, one being an unreacted, and reduced Ga particle, the other possibility could be rooted in the heating process. Since microwave assisted syntheses have an incredibly fast heating profile,[25] Ga could, once reduced, diffuse out of the wire and segregate upon the likewise fast cooling. Similarly, a very recent study by P. Zhang *et al.*[26] describes a comparable phenomenon upon pressureless sintering of bulk Cr_2GaC at higher temperatures (1200–1300 °C), a temperature range very easily accomplished in the microwave system.

The inside of the wires also differs depending on the annealing technique. In FW, Cr is prevalent alongside C in the core region (Fig. S1†), which indicates Cr_3C_2 accumulation inside the wire, which is in line with the XRD data. The carbon content inside the wires is similar to the amounts measured on the surfaces, however, exact quantifications are difficult to achieve due to the glue used to prepare the cross-sectional view (see ESI† for more details). Using the Scherrer equation, grain sizes for Cr_3C_2 were determined to be around 650 nm, meaning the Cr_3C_2 phase visible in Fig. S1† represents accumulations of said phase. MW, on the other hand, are entirely homogeneous throughout the entire cross section (Fig. S3, see ESI† for more details). A potential reason for this difference could stem from the vastly differing heating rates. Particularly the furnace ramping speeds (2 °C per minute) might allow for sufficient crystallite growth and diffusion compared to the drastically faster rates achieved in the microwave oven and result in the differing cross sections. Looking at the different MAX phase grain sizes (also determined by means of XRD), a similar trend is observed: while FW have grain sizes around 190 nm, MW grain sizes amount to only around 70 nm, further supporting the hypothesis of different crystallite growth/mass diffusion rates caused by the different heating techniques.

Electrical properties of Cr_2GaC microwires

As the electronic properties in the mesoscopic range can significantly differ from the bulk counterpart, four-probe resistivity (see Fig. 4a) measurements were performed on individual carbonaceous Cr_2GaC microwires. Our goal was to identify the microscopic processes for electron transport in these composite microwires and to understand how the electronic conduction of the microwires differs from conventional MAX phase systems. Previously reported resistivity (ρ) behavior of pelletized Cr_2GaC has been well-described as a traditional metallic temperature dependence.[27] The overall resistivity decreases monotonically ($d\rho/dT > 0$) as the temperature decreases[27] and is eventually dominated by the defect scattering with signature temperature-independent resistivity at low temperature. Similar responses were also reported for other types of MAX phases and examples include Cr_2GeC,[28] Mn_2GaC,[29] Ti_3AlC_2,[30] and Ti_3SiC_2.[31] On the other hand, graphite, the layered crystalline form of carbon has anisotropic electronic properties due to the presence of van der Waals gap along the crystalline *c*-axis. While the in-plane conduction is dominated by a metallic temperature dependence of resistivity, the out of plane component follows an insulating-like trend with a metal–insulator transition at low temperature.[32]

To do a comparative study, we prepared pellets from elemental precursors grown by both microwave and furnace-based methods and performed four-probe resistivity measurement on them. As shown in Fig. S5,† bulk samples synthesized both in the microwave oven and furnace follow the conventional metallic trend (see ESI for synthesis details and characteriz-

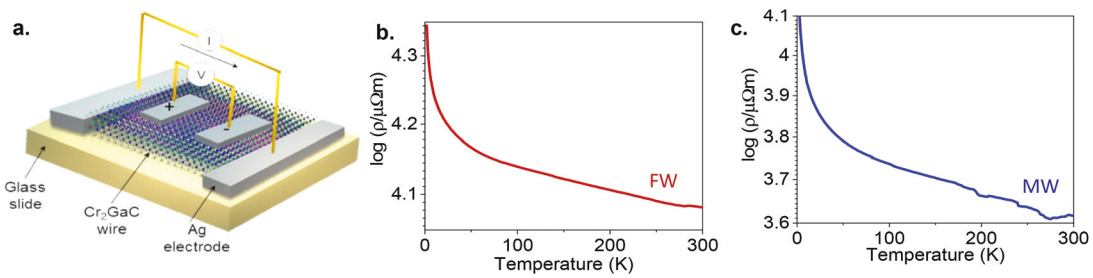

Fig. 4 a. Schematic of four-point-probe resistivity (ρ) measurement performed on Cr_2GaC based carbon microwires; b. log(ρ) *vs.* temperature measurement of a typical furnace-grown carbonaceous Cr_2GaC wire and c. log(ρ) *vs.* temperature curve of a typical microwave-grown wire showing insulating trend.

ation, Fig. S4, Tables S7 and S8†). In contrast to these typical responses from MAX phase pellets, as shown in Fig. 4b and c, the resistivity of carbonaceous Cr_2GaC microwires increases with decreasing temperature for all furnace-derived samples and for a majority of microwave derived samples as opposed to the conventional metallic response. Typical room temperature resistivity values measure in the mΩm range, which is roughly three orders of magnitude higher compared to the reported metallic Cr_2GaC samples.[27] Since the fundamental electronic transport in single crystalline Cr_2GaC is anticipated to be metallic-like (reduced resistivity at low temperature), the observed insulating-like response (increased resistivity at low temperatures) suggests that the electronic transport is dominated by excess amorphous carbon present in the system.

The temperature dependence in Fig. 4b and c can be well fitted to 3D Mott variable range hopping (VRH) model[33,34] given by:

$$\rho(T) = \rho_0 \exp\left(\frac{T_{\text{Mott}}}{T}\right)^{0.25} \quad (1)$$

where ρ_0 is a resistivity prefactor and $T_{\text{Mott}} = A/(k_B N(E_f)\xi^3)$ is the characteristic temperature. Here, A is a prefactor taken as 16, k_B is the Boltzman constant, $N(E_f)$ is the density of states at the Fermi level which varies slowly, and ξ is the electron localization length. The fitting of few FW and the MW to this model using the Levenberg Marquardt algorithm is shown in Fig. S6a and S6b† and it suggests a hopping mechanism at a low-T regime (2 K–170 K). The parameters ρ_0 and T_{Mott} derived from the best fit are listed in Table 1. Using the previously reported $N(E_f)$ value,[35] these fitting results have shown that the localization length ξ is in the range of 5.30–12.74 nm which agrees well with the amorphous character of carbon. These localization length values signify the decay length of the localized wavefunctions. Small values of ξ compared to the wire dimension is indicative of a necessary hopping mechanism for conduction at low T. We also note that the VRH fitting shows a considerable deviation for some cases at higher temperatures as shown in S4a† which can be related to thermally activated conduction processes.[36,37]

While the resistivity of most of the MW obeys the variable range hopping, we found two other responses from a few MW in their ρ *vs.* T, namely "metallic" response (Fig. S6c†) and a combination of metallic and insulating-like behavior (Fig. S6d†). The "metallic" response shown in Fig. S6c† can be attributed to crystalline Cr_2GaC as well as graphitization at high temperature during the synthesis and can be modelled as classical Drude metallic resistivity, *i.e.*, $\rho = \rho_o + \rho_m = \rho_o + A \times T^m$, where ρ_o is the defect and impurity dominated residual resistivity at low temperatures, A is a temperature dependent weight factor and m is temperature dependent exponent related to different scattering mechanisms. Fitting this expression to the metallic ρ *vs.* T data at different temperature ranges produces a set of values of ρ_o, A and m which are reasonable within standard metallic conduction. Analysis of the data at low temperature (11–85 K) shows $m \sim 2.3$. Previously, $m \sim 2$ has been reported for metals where the scattering is due to direct electron–electron (e–e) interaction,[38,39] an Umklapp process with large scattered wavevector,[40] and quantum phase transition (QPT).[41] On the other hand, a T^3 temperature resistivity dependence can be attributed to interband transitions[42] of conduction electrons. Hence, we attribute the $T^{2.3}$ dependence to the interplay of e–e scattering, Umklapp process, and interband scattering of the conduction electrons. The high temperature regime (210–300 K) of the metallic curve gives rise to T-linear dependence which originates from increased electron–phonon interaction at elevated temperature. The scattering phenomena at the intermediate range (85–210 K) are most probably a combination of the low and high-temperature interactions as mentioned above.

The last observed response in MW is non-monotonic behavior, as shown in Fig. S6d,† best described as a transition or cross-over between insulating and metallic-like behavior. One potential reason for such a unique response might be associated with disorder induced multiple scattering in the electronic states near Fermi level (E_f), such as quantum interferences due to weak localization[43,44] and electron–electron interaction in a disordered system.[45,46] Here, another possibility is the series resistivity contribution from insulating-like response

Table 1 Parameters ρ_0 and T_{Mott} obtained from Mott variable range hopping (VRH) fitting of ρ *vs.* T data for insulating-like samples

Synthesis method	Diameter (μm)	Temperature range (K)	ρ_0 (μΩm)	T_{Mott} (K)	R^2	Localization length ξ (nm)
Microwave	73.53 ± 5.90	2–180	2993.92 ± 12.53	12.75 ± 0.26	0.99447	5.30
Furnace	83.16 ± 1.05	2–150	1174.91 ± 6.84	1.71 ± 0.08	0.97509	10.36
Furnace	50.75 ± 1.40	2–300	604.45 ± 0.89	0.92 ± 0.02	0.99449	12.74
Furnace	30.68 ± 1.39	2–300	417.08 ± 1.12	1.16 ± 0.03	0.98823	11.79
Furnace	10.30 ± 0.47	2–124	99.15 ± 0.24	1.04 ± 0.03	0.98110	12.23
Furnace	9.54 ± 0.20	2–300	201.34 ± 0.92	1.06 ± 0.04	0.98745	12.15

Table 2 Parameters σ_o, A and τ derived from $\sigma = \sigma_o + Ae^{-t/\tau}$ fitting to the ρ *vs.* t data of iodinated Cr_2GaC

Wire radius (μm)	Treatment time (h)	σ_0 (S m^{-1})	A (S m^{-1})	τ (h)
35.55 ± 1.68	1.5	3017.90 ± 12.67	7986.20 ± 1101.90	1.4 ± 0.1
21.51 ± 0.67	2	3884.01 ± 23.03	1399.22 ± 269.77	3.4 ± 0.8

(from amorphous carbon) with lower room temperature resistance and metallic-like conduction (from Cr_2GaC) with low ρ_o value. In such a case, as the temperature is lowered, the total resistivity is dominated by the insulating response once the metallic resistivity drops below the insulating range. We note that a similar non-monotonic response has been observed in graphite, graphite-based compounds, and carbon nanotubes and the electrical response still remains open to questions and our studies warrant future studies in the field.[47]

Halide treatment process

Chemical doping is a powerful strategy to improve electrical conductivity. Previously, halide-based doping has been used to engineer the electrical conductivity of carbonaceous materials including graphite,[48] graphene,[49] polymers,[50] and carbon nanotubes.[51] We have employed a halide treatment in a MAX phase based system for the first time to boost their electrical properties. Here, the porous surface and low-dimensionality of carbonaceous MAX phase Cr_2GaC microwires offer large surface to volume ratios and promote greater degrees of interaction with the halides (bromine or iodine vapor). Besides the surface architecture, vdW gaps in amorphous carbon provides ample scope for halogen intercalation between carbon layers. Considering the chemical incompatibility of Au or Ag electrical contacts with the halide vapors, we first subjected the FW microwires to iodine (or bromine) vapor at 200 °C for 1.5 and 2.0 hours (red and blue symbols in Fig. 5c, respectively) and created 4-terminal contacts after the treatment to access their transport properties. Fig. 5a represents a schematic of iodine treatment of Cr_2GaC wires. After the iodine treatment, the presence of iodine in Cr_2GaC MAX phase based wires was confirmed by EDS elemental mappings (Fig. 5b, and S7†). Our estimates from EDS semi-quantitative analysis (Fig. S7†) performed within 2 hours of exposure shows uniform distribution of iodine. The presence of iodine can be further evidenced by the prominent iodine anion Raman peaks located at 101 and 160 cm^{-1} (Fig. 5c), corresponding to the stretching modes of I_3^- and I_5^- anions formed by charge transfer within the carbonaceous Cr_2GaC wire.[52] No Raman peak corresponding to molecular iodine (180 cm^{-1}) eliminates the possibility of iodine accumulation inside the material.

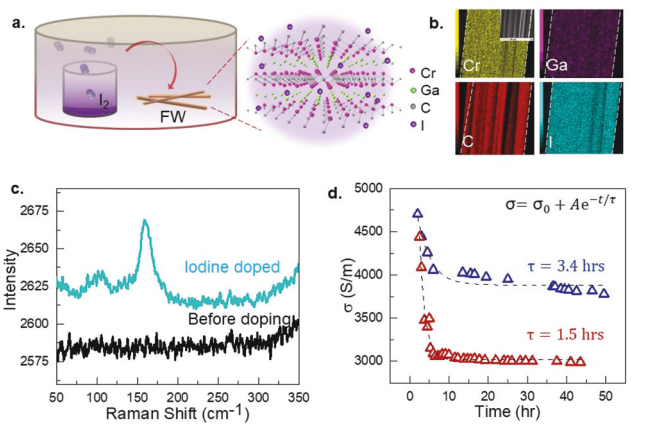

Fig. 5 a. Schematic of iodine treatment in FW b. EDS mapping of Cr, Ga, C and I after iodine treatment in carbonaceous Cr_2GaC microwires; c. Raman spectra before and after iodine treatment; iodine anion peaks are located around 101 cm^{-1} and 160 cm^{-1}; d. Time dependent conductivity of iodinated microwires showing improved conductivity through iodine treatment.

Measurement of time dependent electronic properties after halogen treatment can give insights into the diffusion dynamics of the volatile dopants, which can be useful for gas sensing applications. After the iodine exposure (for bromine, see Fig. S8†), the time-dependent conductivity (Fig. 5d) of the iodinated individual microwires was measured again. Here the time axis refers to the time after the halogen treatment is completed. The overall conductivity increases significantly after halogen treatment and falls with time t following the equation in the form of $\sigma = \sigma_o + Ae^{-t/\tau}$, see fitted curves in dashed lines in Fig. 5d. This clearly indicates that the conductivity of the wires can be improved by a simple post-processing halogen treatment technique. Here, the parameter σ_o is the saturation conductivity. A is the difference between conductivity at time t = 0 and σ_o, and τ correspond to the characteristic time for decay. From A and σ_o values derived from the fitted data, it was found that the conductivity was enhanced by 260% and 36% for two wires shown in Fig. 5d, suggesting halogen diffusion is highly effective in boosting the electrical properties. The parameters obtained from fitting are listed in Table 2. In our experiment, τ changes within the order of hours (Fig. 5d). Since iodine is present inside the wires in anion form, the treatment is likely to increase the conductivity by increasing the overall hole carrier density. As the conductivity shows a time response mainly described by the diffusion process, it also suggests that iodine anions diffuse out of the MAX phase matrix with time coefficients of 1.5 and 3.4 hours. Similar time dependent conductivity data is shown in Fig. S8d.† Though the gas sensing properties of ceramic MAX phase samples are not well explored, this time dependent conductivity response of doped samples makes carbonaceous Cr_2GaC microwires potential candidates for chemiresistive halogen gas sensors.[53]

Conclusion

We report on the first-ever successful synthesis of carbonaceous Cr_2GaC MAX phase microwires, a shape only achievable *via* a modified sol–gel approach. Utilizing conventional furnace heating as well as non-conventional microwave heating, we are able to obtain vastly differing microstructures, especially in terms of surface structure and homogeneity. While furnace-derived microwires exhibit Cr-richer cores and cratered surfaces, microwave-derived microwires appear to be homogenous throughout with smoother and closed surfaces. Leveraging advanced low temperature electronic transport measurements, we discovered transport behavior of the microwires, which ranges from metallic- to insulating-like, as well as combinations thereof. Building on this fundamental under-

standing, we introduced halides (I and Br) into the layered structure of the microwires in order to engineer their electronic properties. Time-resolved measurements revealed a conductivity boost of more than 200%, as well as showed a time-dependent decrease of the boosted conductivity. Based on these findings, we propose MAX phase Cr_2GaC based microwires as (potential) candidates for chemiresistive halogen gas sensors.

Conflicts of interest

There are no conflicts to declare.

Acknowledgements

The authors acknowledge the use of facilities within the Eyring Materials Center at Arizona State University. S. T. acknowledges support from DOE-SC0020653, Applied Materials Inc., NSF CMMI 1825594, NSF CMMI 1933214, NSF CMMI 2129412 and NSF DMR 2111812.

Notes and references

1 M. W. Barsoum, The $M_{N+1}AX_N$ phases: A new class of solids, *Prog. Solid State Chem.*, 2000, **28**, 201–281.
2 M. Radovic and M. W. Barsoum, MAX phases: bridging the gap between metals and ceramics, *Am. Ceram. Soc. Bull.*, 2013, **92**, 20–27.
3 A. Maniv, *et al.*, Microscopic evidence for Mn-induced long range magnetic ordering in MAX phase compounds, *J. Phys.: Condens. Matter*, 2021, **33**, 025803.
4 O. Rivin, *et al.*, Evidence for ferromagnetic ordering in the MAX phase $(Cr_{0.96}Mn_{0.04})_2GeC$, *Mater. Res. Lett.*, 2017, **5**, 465–471.
5 H. Rohde and H. Kudielka, Strukturuntersuchungen an Carbosulfiden von Titan und Zirkon, *Z. Kristallogr. – Cryst. Mater.*, 1960, **114**, 447–456.
6 W. Jeitschko, H. Nowotny and F. Benesovsky, Kohlenstoffhaltige ternäre Verbindungen (H-Phase), *Monatsh. Chem.*, 1963, **94**, 672–676.
7 W. Jeitschko, H. Nowotny and F. Benesovsky, Kohlenstoffhaltige ternäre Verbindungen (V-Ge-C, Nb-Ga-C, Ta-Ga-C, Ta-Ge-C, Cr-Ga-C und Cr-Ge-C), *Monatsh. Chem.*, 1963, **94**, 844–850.
8 J. Etzkorn, M. Ade, D. Kotzott, M. Kleczek and H. Hillebrecht, Ti_2GaC, Ti_4GaC_3 and Cr_2GaC - Synthesis, crystal growth and structure analysis of Ga-containing MAX-phases $M_{n+1}GaC_n$ with M=Ti, Cr and n = 1, 3, *J. Solid State Chem.*, 2009, **182**, 995–1002.
9 Y. Han, *et al.*, Design of Hetero-Nanostructures on MoS_2 Nanosheets to Boost NO_2 Roomerature Sensing, *ACS Appl. Mater. Interfaces*, 2018, **10**, 22640–22649.
10 N. Arya, P. Avasthi and V. Balakrishnan, A light-fostered supercapacitor performance of multi-layered ReS_2 grown on conducting substrates, *Nanoscale Adv.*, 2021, **3**, 2089–2102.
11 Y. H. Wu, T. Yu and Z. X. Shen, Two-dimensional carbon nanostructures: Fundamental properties, synthesis, characterization, and potential applications, *J. Appl. Phys.*, 2010, **108**, 071301-1–071301-38.
12 S. Hong, *et al.*, Highly sensitive active pixel image sensor array driven by large-area bilayer MoS_2 transistor circuitry, *Nat. Commun.*, 2021, **12**, 1–11.
13 S. Balderston, *et al.*, Discrimination of single-point mutations in unamplified genomic DNA via Cas9 immobilized on a graphene field-effect transistor, *Nat. Biomed. Eng.*, 2021, **5**, 713–725.
14 H. Xu, H. Shang, C. Wang and Y. Du, Ultrafine Pt-Based Nanowires for Advanced Catalysis, *Adv. Funct. Mater.*, 2020, **30**, 1–18.
15 M. Law, *et al.*, Nanoribbon waveguides for subwavelength photonics integration, *Science*, 2004, **305**, 1269–1273.
16 Y. S. Zhao, *et al.*, Optical waveguide based on crystalline organic microtubes and microrods, *Angew. Chem., Int. Ed.*, 2008, **47**, 7301–7305.
17 S. H. Lee, *et al.*, Room-Temperature, Highly Durable $Ti_3C_2T_x$ MXene/Graphene Hybrid Fibers for NH3 Gas Sensing, *ACS Appl. Mater. Interfaces*, 2020, **12**, 10434–10442.
18 P. Offermans, M. Crego-Calama and S. H. Brongersma, Functionalized vertical InAs nanowire arrays for gas sensing, *Sens. Actuators, B*, 2012, **161**, 1144–1149.
19 M. Jiang, W. Mao, X. Zhou, C. Kan and D. Shi, Wavelength-Tunable Waveguide Emissions from Electrically Driven Single ZnO/ZnO:Ga Superlattice Microwires, *ACS Appl. Mater. Interfaces*, 2019, **11**, 11800–11811.
20 S. Chen, *et al.*, Ionic liquid-assisted synthesis of N/S-double doped graphene microwires for oxygen evolution and Zn–air batteries, *Energy Storage Mater.*, 2015, **1**, 17–24.
21 G. Y. Chai, *et al.*, Fabrication and characterization of an individual ZnO microwire-based UV photodetector, *Solid State Sci.*, 2011, **13**, 1205–1210.
22 C. M. Hamm, T. Schäfer, H. Zhang and C. S. Birkel, Non-conventional Synthesis of the 413 MAX Phase V_4AlC_3, *Z. Anorg. Allg. Chem.*, 2016, **642**, 1397–1401.
23 C. M. Hamm, J. D. Bocarsly, G. Seward, U. I. Kramm and C. S. Birkel, Non-conventional synthesis and magnetic properties of MAX phases $(Cr/Mn)_2AlC$ and $(Cr/Fe)_2AlC$, *J. Mater. Chem. C*, 2017, **5**, 5700–5708.
24 A. A. Coelho, TOPAS and TOPAS-Academic : an optimization program integrating computer algebra and crystallographic objects written in C++, *J. Appl. Crystallogr.*, 2018, **51**, 210–218.
25 J. P. Siebert, C. M. Hamm and C. S. Birkel, Microwave heating and spark plasma sintering as non-conventional synthesis methods to access thermoelectric and magnetic materials, *Appl. Phys. Rev.*, 2019, **6**, 041314.
26 P. Zhang, *et al.*, Mechanism and mitigation of spontaneous Ga whisker growth on Cr_2GaC, *Sci. China: Technol. Sci.*, 2019, **63**, 440–445.

27 S. Lin, *et al.*, Magnetic and electrical/thermal transport properties of Mn-doped $M_{n+1}AX_n$ phase compounds $Cr_{2-x}Mn_xGaC$ ($0 \leq x \leq 1$), *J. Appl. Phys.*, 2013, **113**, 053502.
28 S. Lin, *et al.*, Alloying effects on structural, magnetic, and electrical/thermal transport properties in MAX-phase $Cr_{2-x}M_xGeC$ (M = Ti, V, Mn, Fe, and Mo), *J. Alloys Compd.*, 2016, **680**, 452–461.
29 I. P. Novoselova, *et al.*, Large uniaxial magnetostriction with sign inversion at the first order phase transition in the nanolaminated Mn_2GaC MAX phase, *Sci. Rep.*, 2018, **8**, 1–11.
30 K. Goc, *et al.*, Structure, morphology and electrical transport properties of the Ti_3AlC_2 materials, *Ceram. Int.*, 2018, **44**, 18322–18328.
31 M. W. Barsoum, *et al.*, Electrical conductivity, thermopower, and Hall effect of Ti_3AlC_2, Ti_4AlN_3, and Ti_3SiC_2, *Phys. Rev. B: Condens. Matter Mater. Phys.*, 2000, **62**, 10194–10198.
32 S. Tongay, *et al.*, Supermetallic conductivity in bromine-intercalated graphite, *Phys. Rev. B: Condens. Matter Mater. Phys.*, 2010, **81**, 1–6.
33 N. F. Mott and E. A. Davis, *Electronic processes in non-crystalline materials*, Oxford Univ. Press, 2012.
34 Y. Sun, *et al.*, Electrical conductivity of single polycrystalline-amorphous carbon nanocoils, *Carbon*, 2016, **98**, 285–290.
35 H. Tong, *et al.*, Difference in physical properties of MAX-phase compounds Cr_2GaC and Cr_2GaN induced by an anomalous structure change in Cr_2GaN, *Intermetallics*, 2019, **105**, 39–43.
36 J. Halim, *et al.*, Variable range hopping and thermally activated transport in molybdenum-based MXenes, *Phys. Rev. B*, 2018, **98**, 1–11.
37 M. Zubair Ansari and N. Khare, Thermally activated band conduction and variable range hopping conduction in Cu_2ZnSnS_4 thin films, *J. Appl. Phys.*, 2015, **117**, 025706-1–025706-7.
38 D. B. Poker and C. E. Klabunde, Temperature dependence of electrical resistivity of vanadium, platinum, and copper, *Phys. Rev. B: Condens. Matter Mater. Phys.*, 1982, **26**, 7012–7014.
39 X. Lin, B. Fauque and K. Behnia, Scalable T2 resistivity in a small single-component Fermi surface, *Science*, 2015, **349**, 945–948.
40 J. R. Wallbank, *et al.*, Excess resistivity in graphene superlattices caused by umklapp electron–electron scattering, *Nat. Phys.*, 2019, **15**, 32–36.
41 J. A. N. Bruin, H. Sakai, R. S. Perry and A. P. Mackenzie, Similarity of Scattering Rates in Metals Showing T-Linear Resistivity, *Science*, 2013, **339**(6121), 804–807.
42 G. W. Webb, Low-temperature electrical resistivity of pure niobium, *Phys. Rev.*, 1969, **181**, 1127–1135.
43 G. Bergmann, Weak localization in thin films, *Phys. Scr.*, 1986, **1986**, 99.
44 R. S. Thompson, D. Li, C. M. Witte and J. G. Lu, Weak Localization and Electron−Electron Interactions in Indium-Doped ZnO Nanowires, *Nano Lett.*, 2009, **9**, 3991–3995.
45 P. Dutta, S. K. Mandal, P. Dey, A. Lakhani and S. M. Yusuf, A comparative study in different rare earth ions in multiferroic nanocomposites: Low temperature resistivity minima and low field magnetoresistance, *J. Magn. Magn. Mater.*, 2020, **502**, 166569.
46 P. A. Lee and T. V. Ramakrishnan, Disordered electronic systems, *Rev. Mod. Phys.*, 1985, **57**, 287–337.
47 J. Fischer, *et al.*, Metallic resistivity in crystalline ropes of single-wall carbon nanotubes, *Phys. Rev. B: Condens. Matter Mater. Phys.*, 1997, **55**, R4921–R4924.
48 J. Li, L. Vaisman, G. Marom and J. K. Kim, Br treated graphite nanoplatelets for improved electrical conductivity of polymer composites, *Carbon*, 2007, **45**, 744–750.
49 S. Majee, D. Banerjee, X. Liu, S. L. Zhang and Z. B. Zhang, Efficient and thermally stable iodine doping of printed graphene nano-platelets, *Carbon*, 2017, **117**, 240–245.
50 S. L. Hsu, A. J. Signorelli, G. P. Pez and R. H. Baughman, Highly conducting iodine derivatives of polyacetylene: Raman, XPS, and X-ray diffraction studies, *J. Chem. Phys.*, 1978, **69**, 106–111.
51 L. Fan and X. Xu, A stable iodine-doped multi-walled carbon nanotube-polypyrrole composite with improved electrical property, *Compos. Sci. Technol.*, 2015, **118**, 264–268.
52 N. Jung, A. C. Crowther, N. Kim, P. Kim and L. Brus, Raman enhancement on graphene: Adsorbed and intercalated molecular species, *ACS Nano*, 2010, **4**, 7005–7013.
53 S. J. Kim, *et al.*, Metallic $Ti_3C_2T_x$ MXene Gas Sensors with Ultrahigh Signal-to-Noise Ratio, *ACS Nano*, 2018, **12**, 986–993.